ChemPhysChem

Chemistry Europe
European Chemical Societies Publishing

Accepted Article

Title: Ether-functionalized Pyrrolidinium-based Room Temperature Ionic Liquids: Physicochemical Properties, Molecular Dynamics, and the Li ion Coordination Environment

Authors: Kazuki Yoshii, Takuya Uto, Takakazu Onishi, Daichi Kosuga, Naoki Tachikawa, and Yasushi Katayama

To be cited as: *ChemPhysChem* 10.1002/cphc.202100380

Link to VoR: https://doi.org/10.1002/cphc.202100380

WILEY-VCH

WILEY-VCH

FULL PAPER

Ether-functionalized Pyrrolidinium-based Room Temperature Ionic Liquids: Physicochemical Properties, Molecular Dynamics, and the Li ion Coordination Environment

Kazuki Yoshii,*[a][b] Takuya Uto,*[c] Takakazu Onishi,[d] Daichi Kosuga,[b] Naoki Tachikawa,[b] and Yasushi Katayama[b]

[a] Dr. K. Yoshii
Department of Energy and Environment, Research Institute of Electrochemical Energy (REICEN),
National Institute of Advanced Industrial Science and Technology (AIST),
1-8-31 Midorigaoka, Ikeda, Osaka 563-8577, Japan
E-mail: k.yoshii@aist.go.jp

[b] Dr. K. Yoshii, D. Kosuga, Dr. N. Tachikawa, Prof. Dr. Y. Katayama
Department of Applied Chemistry, Faculty of Science and Technology,
Keio University
3-14-1 Hiyoshi, Kohoku-ku, Yokohama, Kanagawa 223-8522, Japan

[c] Dr. T. Uto
Organization for Promotion of Tenure Track,
University of Miyazaki,
Nishi 1-1 Gakuen-Kibanadai, Miyazaki 889-2192, Japan
E-mail: t.uto@cc.miyazaki-u.ac.jp

[d] T. Onishi
Graduate School of Engineering,
University of Miyazaki,
Nishi 1-1 Gakuen-Kibanadai, Miyazaki 889-2192, Japan

Supporting information for this article is given via a link at the end of the document.

Abstract: The physicochemical properties of room temperature ionic liquids (RTILs) consisting of bis(trifluoromethanesulfonyl)amide ($TFSA^-$) combined with 1-hexyl-1-methylpyrrolidinium ($Pyr_{1,6}^+$), 1-(butoxymethyl)-1-methylpyrrolidinium ($Pyr_{1,1O4}^+$), 1-(4-methoxybutyl)-1-methyl pyrrolidinium ($Pyr_{1,4O1}^+$), and 1-((2-methoxyethoxy)methyl)-1-methylpyrrolidinium ($Pyr_{1,1O2O1}^+$) were investigated using both experimental and computational approaches. $Pyr_{1,1O2O1}TFSA$, which contains two ether oxygen atoms, showed the lowest viscosity, and the relationship between its physicochemical properties and the position and number of the ether oxygen atoms was discussed by a careful comparison with $Pyr_{1,1O4}TFSA$ and $Pyr_{1,4O1}TFSA$. *Ab initio* calculations revealed the conformational flexibility of the side chain containing the ether oxygen atoms. In addition, molecular dynamics (MD) calculations suggested that the ion distributions have a great impact on the transport properties. Furthermore, the coordination environments of the Li ions in the RTILs were evaluated using Raman spectroscopy, which was supported by MD calculations using 1000 ion pairs. The presented results will be valuable for the design of functionalized RTILs for various applications.

1. Introduction

Room temperature ionic liquids (RTILs), which are salts that adopt a liquid state below 100 °C, show unique physicochemical properties, such as non-flammability, chemical stability, a negligible vapor pressure, and a relatively high ionic conductivity. These features lead to a wide variety of research into RTILs for their application in energy storage devices, biomass production, gas separation, organic synthesis, and so on.[1–7] The bulk physicochemical properties of RTILs, such as their density, viscosity, and ionic conductivity, are known to depend significantly on the combination of the compositional cation and anion. Among the various RTILs reported to date, RTILs consisting of pyrrolidinium cations are known to exhibit relatively low viscosities and high ionic conductivities when combined with amide-based anions, such as bis(trifluoromethanesulfonyl)amide ($TFSA^-$) or bis(fluoromethanesulfonyl)amide (FSA^-).[8–10] Although the pyrrolidinium-based RTILs are more viscous than those based on imidazolium due to their higher electrochemical stabilities, they have been widely studied as electrolytes in the field of electrochemistry.[11, 12]

The physicochemical properties of RTILs can be tuned by introducing a functional group into the side chain of the cation. It is known that replacing methylene groups with ether oxygen-containing groups yields RTILs with lower viscosities and higher ionic conductivities.[13–17] For example, in the case of ammonium cations, it has been reported that the physicochemical properties of RTILs change depending on how the two ether oxygen species are introduced.[17] In pyrrolidinium-based RTILs, many RTILs containing ether oxygen atoms have been reported, and their resulting physicochemical properties based on the introduction of ether oxygen atoms into the side chains have been investigated using both experimental and computational approaches.[16,18–23] However, few systematic studies have been carried out into the effects of the oxygen atom position on the physicochemical properties of these RTILs.[20–22] In this context, our group recently clarified the correlation between the physicochemical properties and the number of methylene groups between the ether oxygen atom in the side chain and the nitrogen atom in the pyrrolidinium ring by a combination of experiments and molecular dynamics (MD) simulations.[22] We also reported that heterogeneous ion distribution caused by the introduction of ether oxygen atoms into

the side chains leads to good transport properties. Thus, to design RTILs that exhibit the desired properties, it is important to investigate the correlation between their physicochemical properties and the cation structure in a detailed and systematic manner.

RTILs containing ether oxygen atoms have been investigated for use as electrolytes in energy storage devices due to their relatively high ionic conductivities. Furthermore, it has been reported that the interaction of the cation with the ether oxygen atom can change the solvation state of the metal ion, thereby promoting electrochemical reactions.[19, 24–26] When a Li ion is dissolved in TFSA-based RTILs without a heteroatom in the side chain, a $[Li(TFSA)_2]^-$ complex is formed in the mixture.[27–29] On the other hand, in RTILs that contain ether oxygen atoms, it has been reported that the nucleophilicity of the ether oxygen atom affects the coordination environment of the Li ion.[24–26] The interaction of the cation side chain with the metal ion and the application of such species in electrochemical reactions has also been investigated using Na^+, Zn^{2+}, Mg^{2+}, and Ca^{2+} ions, among others.[30–33] In the context of electrolyte design, it is therefore desirable to understand the coordination environments of the metal ions present in RTILs.

As shown in Fig. 1, in a previous study, we investigated RTILs in which the ether oxygen atom was introduced into propyl and butyl groups. In the present study, we focus on RTILs bearing a hexyl group, and prepare RTILs containing one or two ether oxygen substituents to investigate the influences of the number and position of the oxygen atoms on the physicochemical properties. Four pyrrolidinium-based RTILs consisting of bis(trifluoromethanesulfonyl)amide ($TFSA^-$) combined with 1-hexyl-1-methylpyrrolidinium ($Pyr_{1,6}^+$), 1-(butoxymethyl)-1-methylpyrrolidinium ($Pyr_{1,1O4}^+$), 1-(4-methoxybutyl)-1-methyl pyrrolidinium ($Pyr_{1,4O1}^+$), and 1-((2-methoxyethoxy)methyl)-1-methylpyrrolidinium ($Pyr_{1,1O2O1}^+$) were prepared. Upon increasing the length of the side chain (i.e., from propyl or butyl to hexyl), the possible number of stable structures should be increased, and the effect of the introduced ether oxygen atom on the physicochemical properties is expected to be more pronounced. The physicochemical properties of the prepared RTILs are then investigated rigorously using an experimental approach, while *ab initio* and MD calculations are performed to discuss the effects of the position and number of ether oxygen atoms on the RTILs. We also evaluate the physicochemical properties of the prepared RTILs using LiTFSA, and examine the coordination environments of the Li ions in the RTILs.

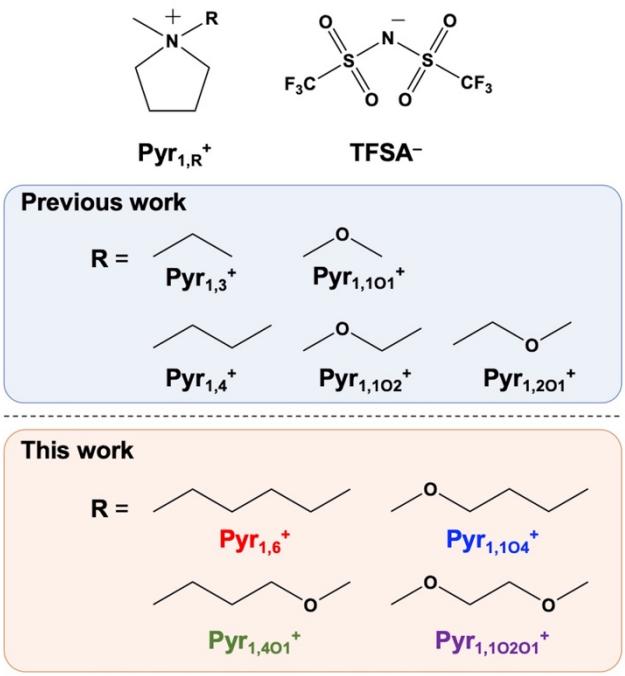

Figure 1. Chemical structures of the cations and anions of the RTILs of our previous and present studies.

2. Results and Discussion

2.1 Physicochemical properties of the RTILs

To the best of our knowledge, although the preparation and a part of physicochemical properties of $Pyr_{1,6}$TFSA and $Pyr_{1,1O2O1}$TFSA have been reported,[34,35] those of $Pyr_{1,1O4}$TFSA and $Pyr_{1,4O1}$TFSA have not. The physicochemical properties of these four RTILs were therefore evaluated under an inert atmosphere. Their glass transition temperatures (T_g) and melting temperatures (T_m) were measured by differential scanning calorimetry (DSC), as listed in Table 1 and shown in Figure S1. It was found that $Pyr_{1,6}$TFSA and $Pyr_{1,4O1}$TFSA exhibit their T_m after their T_g and cold crystallization temperatures (T_c), whereas $Pyr_{1,1O4}$TFSA and $Pyr_{1,1O2O1}$TFSA exhibited only a T_g. This result indicates that $Pyr_{1,6}$TFSA and $Pyr_{1,4O1}$TFSA more readily adopt a packing structure in the lower temperature range compared to $Pyr_{1,1O4}$TFSA and $Pyr_{1,1O2O1}$TFSA. The structural differences between these RTILs relate to the position of the ether oxygen atom, wherein a greater structural flexibility can be expected when the ether oxygen atom is located close to the nitrogen atom of the pyrrolidinium ring.

Figure 2 shows the temperature dependence of the densities (ρ (g cm^{-3})) of the four pyrrolidinium-based RTILs, wherein a linear dependence was observed for all RTILs. The density was fitted by the following equation:

$$\rho = a + bT \quad (1)$$

The parameters fitted by the least-square method are summarized in Table S1 along with the coefficient of determination (R^2) for the fitting. As can be seen from the obtained data, the density decreased in the order of $Pyr_{1,1O2O1}$TFSA > $Pyr_{1,4O1}$TFSA > $Pyr_{1,1O4}$TFSA > $Pyr_{1,6}$TFSA. This result indicates

that the introduction of ether oxygen atoms into the side chain increased the density. Comparing $Pyr_{1,4O1}TFSA$ and $Pyr_{1,1O4}TFSA$, which have the same molecular weight and are structural isomers, the density was higher when the ether oxygen atom was located further from the pyrrolidinium ring. This may reflect the differences in the possible stable cation structures depending on the position of the ether oxygen atom in the side chain,[20, 22, 36] as will be discussed in detail later based on the results of MD calculations.

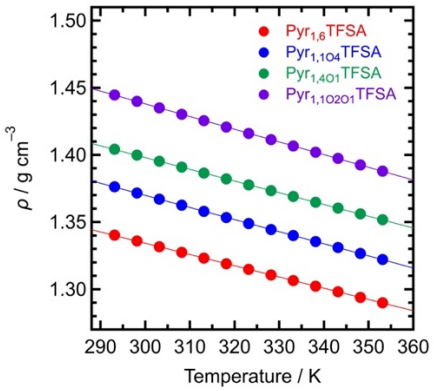

Figure 2. Temperature dependence of the density for the four pyrrolidinium-based RTILs.

Table 1. Physicochemical properties of the pyrrolidinium-based RTILs

RTILs	FW[a]	T_g / K [b]	T_m / K [c]	ρ / g cm^{-3} [d]	C_M / mol L^{-1} [e]	η / mPa s [f]	σ / mS cm^{-1} [g]	κ / S cm^2 mol^{-1} [h]
$Pyr_{1,6}TFSA$	450.5	190.5	275.9	1.336	2.97	107	1.4	0.47
$Pyr_{1,1O4}TFSA$	452.4	173.8		1.372	3.03	49.9	2.9	0.96
$Pyr_{1,4O1}TFSA$	452.4	191.0	250.9	1.400	3.09	81.3	1.9	0.61
$Pyr_{1,1O2O1}TFSA$	454.4	183.0		1.440	3.17	44.4	3.8	1.2

[a] Formula weight. [b] Glass transition temperature. [c] Melting temperature. [d] Density at 298 K. [e] Molar concentration as calculated from the formula weight and density at 298 K. [f] Viscosity at 298 K. [g] Conductivity at 298 K. [h] Molar conductivity at 298 K.

Figure 3a shows the temperature dependence of the viscosity (η (mPa s)) for the RTILs. Since the plot exhibited a concave profile, Arrhenius equation cannot be used for the fitting. Therefore, the data were fitted by the Vogel-Tamman-Fulcher (VTF) equation shown below:[37]

$$\eta = \eta_0 T^{1/2} \exp\left[B/(T - T_o)\right] \quad (2)$$

where B (K) is a constant related to the Arrhenius activation energy for the viscous behavior, T_0 (K) is the ideal glass transition temperature, and η_0 is a scaling factor. The fitted parameters are summarized in Table S2. It was found that $Pyr_{1,1O4}TFSA$ and $Pyr_{1,1O2O1}TFSA$ showed lower viscosities compared to the other two RTILs. This result, i.e., the fact that the RTIL with a smaller number of methylene groups between the ether oxygen and nitrogen atoms showed a lower viscosity, is consistent with previous reports.[22] The lower viscosity of $Pyr_{1,1O2O1}TFSA$, which contained two ether oxygen atoms was attributed to the higher structural flexibility of its side chain compared to the systems with only one ether oxygen atom.

Figure 3b shows the temperature dependence of the ionic conductivity (σ (mS cm^{-1})) for the RTILs. The VTF equation for the conductivity is:

$$\sigma = \sigma_0 T^{-1/2} \exp\left[-B/(T - T_o)\right] \quad (3)$$

where σ_0 is a scaling factor. The fitted parameters are summarized in Table S3. As indicated, the ionic conductivity was consistent with the order of viscosity, with $Pyr_{1,1O2O1}TFSA$, which had the lowest viscosity, showing the highest ionic conductivity. This result indicates that the ionic conductivity is mainly influenced by the viscosity, as expected according to Walden's rule.[38] The molar ionic conductivities are also listed in Table 1, and these values were found to follow the same order as the ionic conductivity.

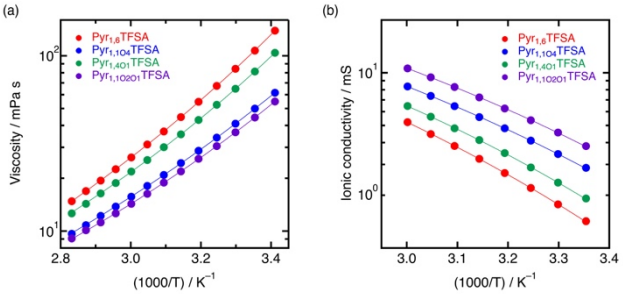

Figure 3. Temperature dependence of (a) the viscosity, and (b) the ionic conductivity for the four pyrrolidinium-based RTILs.

2.2 *Ab initio* quantum mechanics (QM) calculations

To understand the differences in the physicochemical properties evoked by the position and number of ether oxygen atoms in the cation side chain, the optimized structures of the pyrrolidinium cation conformers were calculated by *ab initio* quantum mechanics (QM) calculations. It is well known that the pseudo

rotation of the pyrrolidine ring gives many conformers, including envelope and twist structures.[39] Thus, the calculation was performed using the initial structure with the methyl group in the axial position of the plane composed of the nitrogen atom and four carbon atoms. Figure 4 shows the most stable local structure obtained by the calculation at the MP2/aug-cc-pVTZ//MP2/6-31G(d,p) level of theory. The values of the dihedral angles of the various cations are listed in Table S4, and the dihedral angles (Φ_1 to Φ_4) are defined as depicted in Fig. S2. $Pyr_{1,6}^+$, which contains no ether oxygen atom in its side chain, exhibited the all-*trans* conformation in its alkyl chain. In contrast, the other three cations, which contained ether oxygen atom, exhibited the folded form, with the oxygen atom facing the pyrrolidinium ring. More specifically, $Pyr_{1,4O1}^+$ and $Pyr_{1,1O2O1}^+$ were considered to exhibit the folded form due to hydrogen bonding between the ether oxygen atom and the pyrrolidinium ring.[15] In contrast, $Pyr_{1,1O4}^+$ showed a different conformational behavior to $Pyr_{1,6}^+$, despite the fact that it appears to contain no intramolecular hydrogen bonds.

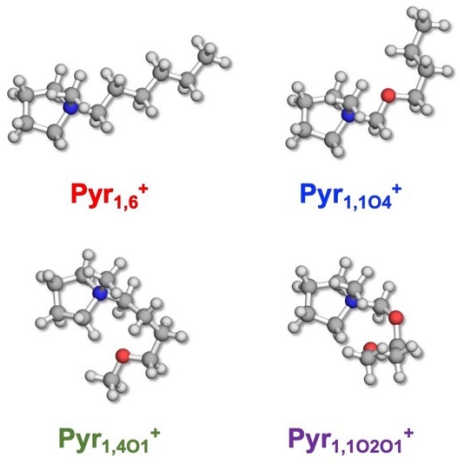

Figure 4. Optimized structures of the pyrrolidinium cations calculated at the MP2/6-31G(d,p) level theory. The most stable structures obtained from the conformational analyses are shown.

The calculated torsional potentials for Φ_1 to Φ_4 (defined in Fig. S2) are shown in Fig. 5, where the potential energy was defined as the difference in potential energy relative to the minimum energy value. $Pyr_{1,6}^+$ and $Pyr_{1,4O1}^+$ showed minimal energies when Φ_1 was 180°, and in the gauche conformation when Φ_1 was close to ±60°. $Pyr_{1,1O4}^+$ and $Pyr_{1,1O2O1}^+$, which possess an ether oxygen atom close to the pyrrolidinium ring, were most stable at Φ_1 values of 180 and 90°, respectively. In these cations, we confirmed that the potential barrier of Φ_1 was low between 180 and ±90°, indicating that the dihedral angle of Φ_1 can easily transform the conformation when the ether oxygen atom is located close to the pyrrolidinium ring. In Φ_2, the potential barrier was lower compared to those of the other dihedral angles. For $Pyr_{1,4O1}^+$ and $Pyr_{1,1O2O1}^+$, which possess oxygen atoms located far from the pyrrolidinium ring, the energy minimum points were confirmed at the dihedral angle corresponding to an eclipsed conformation (i.e., Φ_2 = ±60, ±120, and ±135°). In the most stable cation structure with an exhaustive variation of the Φ_1 to Φ_4 values shown in Fig. 4, these two cations exhibited the eclipsed conformation at Φ_1 and Φ_2, respectively. The bending of the cation side chain was considered to contribute to stabilization of the intramolecular interactions with the pyrrolidinium ring. In Φ_3, each cation showed a minimum energy point at approximately ±60°. In Φ_4, each cation showed a minimum energy point at approximately ±180°. $Pyr_{1,6}^+$ and $Pyr_{1,1O4}^+$ exhibited the gauche conformation close to ±60°. The biggest difference in the potential energy barrier of the dihedral angle was observed at Φ_1, which corresponds to the root of the cation side chain. From this result, we can conclude that the potential energy barrier of Φ_1 is one of the factors that causes $Pyr_{1,1O4}$TFSA and $Pyr_{1,1O2O1}$TFSA to exhibit low viscosities and high ionic conductivities. The above results suggest that $Pyr_{1,1O2O1}$TFSA showed the best transport properties among the four RTILs due to the fact that $Pyr_{1,1O2O1}$TFSA allows the eclipsed conformation (±90°) at Φ_1, and gives a wider range of conformations than $Pyr_{1,1O4}$TFSA. Moreover, $Pyr_{1,4O1}$TFSA, which showed the same bending structure as $Pyr_{1,1O2O1}$TFSA, exhibited the characteristic energy profiles of Φ_2 and Φ_3. However, Φ_1 was more restricted than in the case of $Pyr_{1,1O4}$TFSA, and so it is reasonable to assume that the transport properties of $Pyr_{1,4O1}$TFSA are inferior to those of $Pyr_{1,1O4}$TFSA. Focusing on Φ_1, similar potential profiles were obtained in $Pyr_{1,6}^+$ and $Pyr_{1,4O1}^+$, but $Pyr_{1,4O1}$TFSA was more likely to give the *gauche* configuration. As pointed out in our previous study,[22] the introduction of ether oxygen atoms to improve the transport properties could be explained in terms of the flexibility of the steric conformation. We also reported that the most stable structures of $Pyr_{1,1O1}$TFSA and $Pyr_{1,1O2}$TFSA were the all-*trans* conformations of the side chains, whereas $Pyr_{1,1O4}$TFSA showed the *gauche* conformation of Φ_3 in the most stable structure, despite the fact that it showed no side chain bending. This may be due to the contribution of the stereoelectronic effect,[40] suggesting that the length of the alkoxy chain also influences the physicochemical properties.

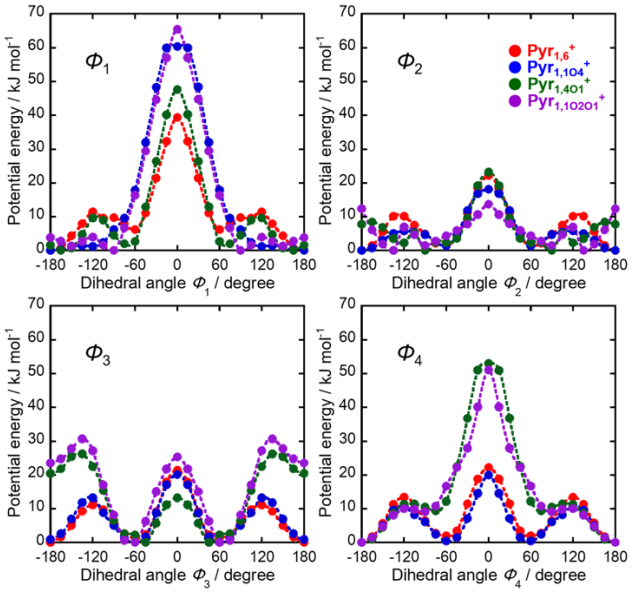

Figure 5. Potential energy surfaces for the dihedral angles (Φ_1, Φ_2, Φ_3, and Φ_4) of the four cations. The potential energy is defined as the difference between the potential energy and the minimal energy value obtained by QM calculations at the MP2/aug-cc-pVTZ//MP2/6-31G(d,p) level of theory.

2.3 Molecular dynamics (MD) simulations

The potential energy surfaces for the dihedral angles of the cation side chains were then evaluated by QM calculations, and the physicochemical properties were discussed in terms of the conformational flexibility. Furthermore, MD calculations were performed to analyze the dynamic behaviors of the pyrrolidinium-based RTILs in the condensed systems at 300 K. Figure S3 displays the probability distribution of the dihedral angles (Φ_1–Φ_2, Φ_2–Φ_3, and Φ_3–Φ_4) for the four cations based on MD trajectories of 1 μs. As indicated, the Φ_1–Φ_2 profiles of $Pyr_{1,1O4}^+$ and $Pyr_{1,1O2O1}^+$ were widely distributed, indicating that various conformations were present even in their condensed systems, and this result supports those obtained by QM calculations. On the other hand, the Φ_1–Φ_2 profiles of $Pyr_{1,6}^+$ and $Pyr_{1,4O1}^+$ showed a narrow distribution range. In addition, the Φ_2–Φ_3 and Φ_3–Φ_4 profiles gave different distributions among the four types of RTILs. $Pyr_{1,1O2O1}^+$ took only the gauche conformation for the Φ_3 angle in its bending form. Figure 6 shows a histogram representation the variation in the length between the cation center and the side chain end for the four RTILs in terms of the tail length. The tail length profile of $Pyr_{1,1O2O1}^+$ showed a wide distribution due to the flexibility of the conformation, and some distributions within 0.5 nm were reflected by the bent morphology. The various morphologies of the cation side chain in $Pyr_{1,1O2O1}$TFSA were also observed, as shown in the MD snapshot (Fig. S4). Although $Pyr_{1,1O4}^+$, which possesses a flexible Φ_1 angle, also gave a slightly wider distribution, the side chain did not bend (Fig. S4). Moreover, the tail length profiles of $Pyr_{1,6}^+$ and $Pyr_{1,4O1}^+$ showed well-defined peaks, reflecting rigid side chain morphologies in both cases.

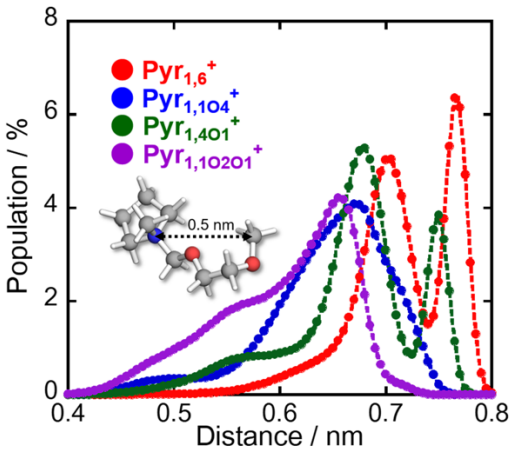

Figure 6. Distribution profiles of the intramolecular center-to-end distances for the four cations as obtained from MD trajectories of 1 μs.

The experimental data obtained for the densities of the four RTILs could be qualitatively reproduced by the MD calculations, which confirms the validity of the revised force field parameters (Fig. S5). In the case of $Pyr_{1,1O2O1}$TFSA, which showed the highest density among the four RTILs, a bent morphology was observed for the cation side chain, in addition to the approach between the cations (Fig. S4). Therefore, the radial distribution function (RDF) was analyzed to evaluate the ion-ion interactions. $Pyr_{1,6}$TFSA displayed the largest peak in the RDF profile between the cation center (nitrogen atom) and the anion (oxygen atom), indicating the strongest cation-anion interaction (Fig. 7a). There was little difference in the RDF profiles for the interactions between the cation side chain and the anion (Fig. 7b), and the RDF profiles between the cation–cation pairs (Figs. 7c and 7d) showed that the $Pyr_{1,1O2O1}^+$–$Pyr_{1,1O2O1}^+$ distance was the shortest among the RTILs, thereby resulting in weakened cation-anion interactions in the case of $Pyr_{1,1O2O1}$TFSA. For the RTILs possessing an ether oxygen atom in the side chain, the cation–anion repulsion may also affect the physical properties (Fig. 7a). Furthermore, the introduction of an ether oxygen atom on the side chain could improve the accessibility between cations due to interactions between the cation center and the side chain end (Fig. S4). The order of approach distance ranked by the RDF profiles between the cations was found to correspond to the densities of RTILs (Figs. 7c and 7d), and the liquid densities of the pyrrolidinium-based RTILs could be explained by the cation–cation interactions, as proposed in our previous study. Since the density of $Pyr_{1,1O2O1}$TFSA is relatively higher compared to the corresponding values for the other RTILs, it was considered that the contribution of the excluded volume derived from the bent morphology of the cation side chain also affected the liquid density of $Pyr_{1,1O2O1}$TFSA.

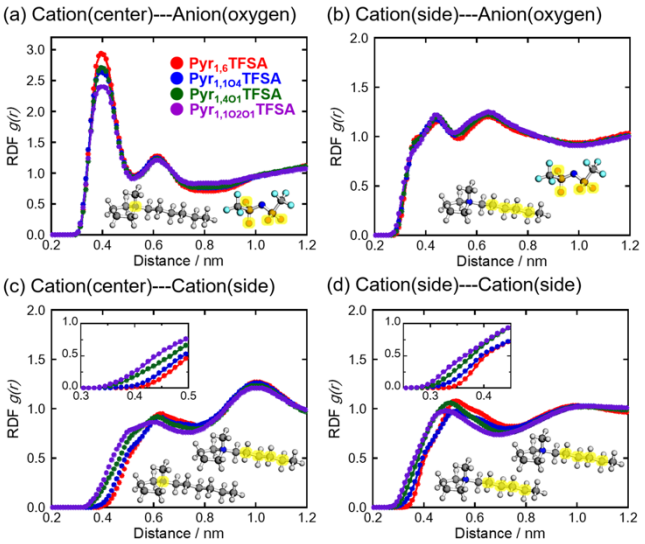

Figure 7. Radial distribution function g(r) involving the cation-anion (top) and the cation-cation (bottom) interactions between the highlighted parts of the four RTILs, as determined by MD trajectories of 1 μs.

$Pyr_{1,4O1}$TFSA gave the second closest distance between cations among the four RTILs, but the cation-anion interaction was stronger than in the case of $Pyr_{1,1O4}$TFSA, and this is expected to be related to the transport characteristics. Figure 8 shows the mean square displacement (MSD) profiles of the RTILs, which is an index of the transport properties. The self-diffusion coefficients are determined by the slopes of the MSD plots obtained from the Einstein relationship. As indicated, $Pyr_{1,6}$TFSA and $Pyr_{1,4O1}$TFSA exhibited lower diffusivities than the other RTILs, as in the case of their viscosities and ionic conductivities. On the other hand, $Pyr_{1,1O4}$TFSA and $Pyr_{1,1O2O1}$TFSA, which contain ether oxygen atoms in their cation side chains, exhibited good transport properties, thereby suggesting that their dynamic properties are strongly affected by the position of the ether oxygen atom. To evaluate the transport properties in terms of the ion arrangement, the distributions of the ions around the cation in the 3D space

were determined, as shown in Fig. 9. These results suggest that the transport properties of the RTILs corresponded to the space occupancies in the high-density regions of ions. $Pyr_{1,6}$TFSA and $Pyr_{1,4O1}$TFSA showed regular and uniform ion distributions, resulting in high melting points. The phase transitions for $Pyr_{1,6}$TFSA and $Pyr_{1,4O1}$TFSA were also observed, and these reflected the ordered structure of the ion arrangement in the DSC measurements (Fig. S1). Moreover, it was found that the transport properties of $Pyr_{1,4O1}$TFSA were affected by the regular arrangement of ions derived from cation-cation and cation-anion interactions, as shown by the RDF profiles. On the other hand, it was suggested that $Pyr_{1,1O4}$TFSA and $Pyr_{1,1O2O1}$TFSA possess narrow anion distributions, and disturb the regularity of the ion arrangement due to the flexibility of the side chain. The present study is focused on the $TFSA^-$, but of course, the ion distribution is expected to change depending on the type of anion.[41] This is an important point for the design of the electrolyte and a subject for the future study.

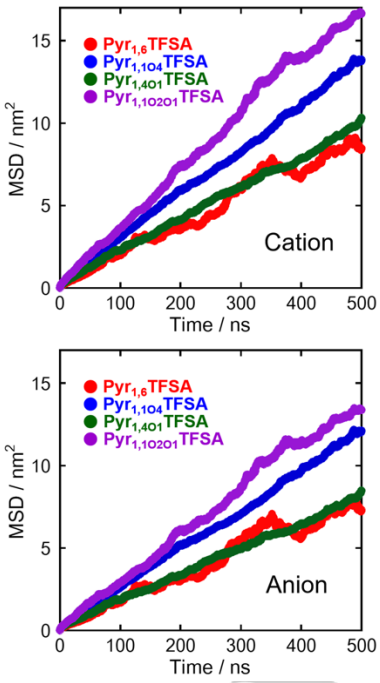

Figure 8. Mean square displacements (MSDs) of the cations and anions in the four RTIL systems calculated using MD trajectories of 500 ns.

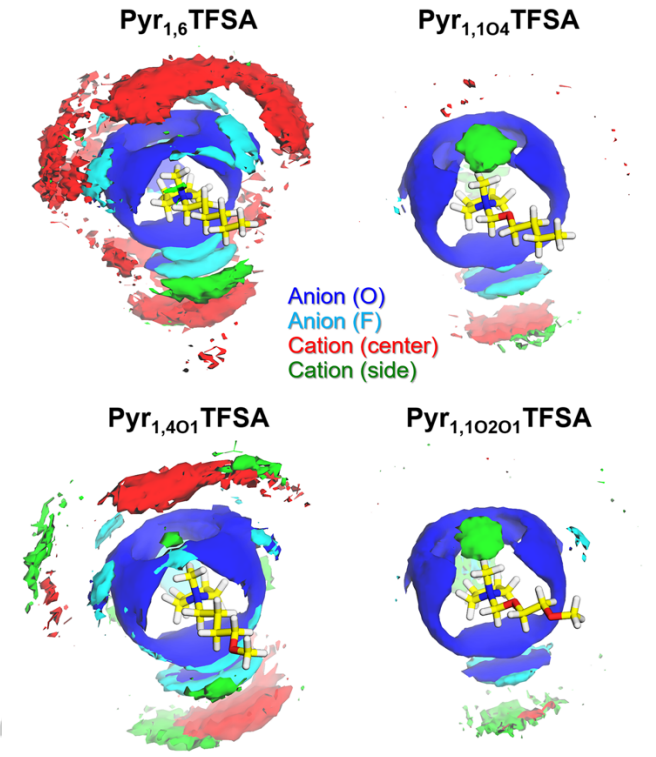

Figure 9. Isocounter surfaces of the cation and anion densities relative to the structures of the pyrrolidinium-based cations, calculated from MD trajectories of 1 μs. Blue and cyan surfaces indicate the high-density distributions of the anions corresponding to 2 times the bulk densities of oxygen and fluorine, respectively. Green and red surfaces indicate the high-density distributions of the cations corresponding to 1.5 times the bulk densities of the cation-center and the side chain, respectively. The density was calculated for a 0.05 × 0.05 × 0.05 nm grid as the number of hits in 2,000,000 frames.

2.4 Physicochemical properties of the RTILs in the presence of LiTFSA, and evaluation of the coordination environment of the lithium ion

Considering the application of RTILs for the electrolytes of Li ion batteries, it is necessary to understand the transport properties of RTILs containing Li ions. It has been also suggested that the Li ion coordination environment in each RTIL depends on the structure of the cation, and the effect of the solvation state on the electrochemical reaction has been investigated.[25, 32, 33] Thus, the physicochemical properties of the RTILs in the presence of Li ions were measured by dissolving 0.2, 0.4, 0.6, 0.8, and 1.0 M LiTFSA in each RTIL. Figure 10 shows the densities, viscosities, and ionic conductivities of the RTILs with each concentration of Li. More specifically, the densities of all RTILs increased as the Li concentration increased, and the viscosity showed a similar trend. Interestingly, when $Pyr_{1,1O4}$TFSA and $Pyr_{1,1O2O1}$TFSA were compared, the viscosity of $Pyr_{1,1O2O1}$TFSA, which contains two ether oxygen atoms in the side chain, became larger as the Li concentration increased. This was considered to affect the coordination environment of the Li ions in $Pyr_{1,1O2O1}$TFSA. It was also found that the ionic conductivity decreased as the Li concentration increased, as confirmed by the change in viscosity.

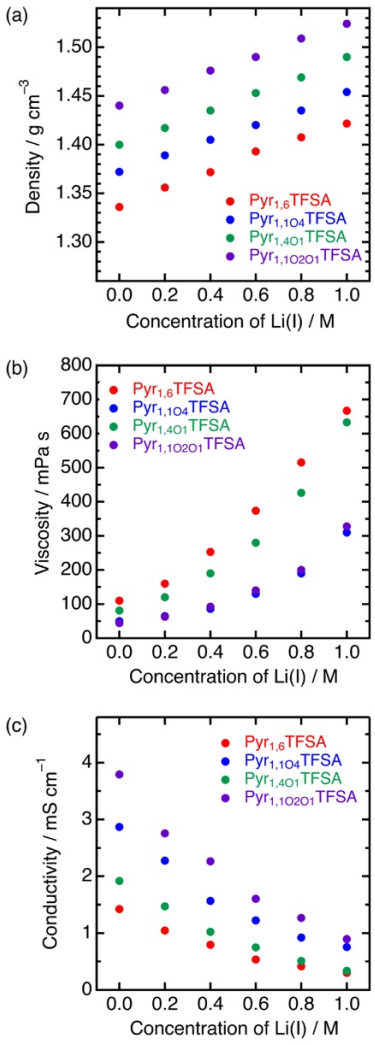

Figure 10. Dependence of the (a) density, (b) viscosity, and (c) ionic conductivity on concentration of Li^+ in the four pyrrolidinium-based RTILs.

It is well known that when LiTFSA is dissolved in TFSA-based RTILs, the Li ion coordinates to the oxygen atom derived from $TFSA^-$ to form the $[Li(TFSA)_n]^{1-n}$ complex.[27–29] The solvation number (*n*) of the Li ion in 1-butyl-3-methylimidazolium TFSA has been reported to be 2, and this value varied in the presence of different metal ions.[28, 42] The coordination environment of the Li ion has been also investigated in pyrrolidinium-based RTILs, and it was pointed out that the aggregation of cations with longer alkyl side chains affected the solvation state of the Li ion.[18, 19, 43–45] The coordination environment of the Li ion in a number of RTILs bearing ether oxygen atoms in their side chains has also been analyzed, although its dependence on the position and number of the ether oxygen atoms has yet to be discussed sufficiently.[18, 19, 25, 31, 46] Thus, Figs. 11(a)–11(d) show the Raman spectra of the four prepared RTILs containing 1.0 M LiTFSA, wherein the two peaks can be fitted using the Voigt function. More specifically, the peak at ~742 cm^{-1}, which was assigned to the CF_3 bending vibration, combined with that of the S-N stretching vibration of $TFSA^-$. It is also well known that the peak observed at a higher wavenumber can be assigned to the anion bound to the metal cation when the corresponding metal TFSA salt is dissolved in RTIL.[27, 28] Upon comparison of the four RTILs with 1.0 M LiTFSA added, the intensity of the peak corresponding to $TFSA^-$ solvated with Li was greater than that corresponding to the free $TFSA^-$ for Pyr$_{1,6}$TFSA and Pyr$_{1,1O4}$TFSA, while the opposite behavior was observed for Pyr$_{1,4O1}$TFSA and Pyr$_{1,1O2O1}$TFSA. This difference was considered to be due to structural differences in the side chains of the cations. Subsequently, the peak intensities of the free $TFSA^-$ (I_{free}) and the $TFSA^-$ solvated with Li ions (I_{solve}) were calculated from the fitting of the Raman spectra of each RTIL with added 0.2, 0.4, 0.6, 0.8, and 1.0 M LiTFSA and plotting against the molar fraction of lithium ions in the RTILs (Fig. 11(e)).[25, 47] Lines with slopes of n = 1 and 2 were drawn for comparison, where n denotes the solvation number of $TFSA^-$. This analysis was conducted under the assumption of an unchanged Raman activity for both I_{free} and I_{solve}. Thus, Pyr$_{1,6}$TFSA and Pyr$_{1,1O4}$TFSA showed a solvation number close to 2, whereas the slopes of the plots for Pyr$_{1,4O1}$TFSA and Pyr$_{1,1O2O1}$TFSA were less steep, and the solvation number was close to 1. This result indicates that the ether oxygen atom in the side chain was involved in the solvation of the Li ion, and that the number and position of ether oxygen atoms was significant for the solvation state. The coordination environment of the Li ion in piperidinium-based RTILs containing ether oxygen atoms has been previously discussed in the literature,[25] wherein the opposite trend was observed, i.e., the solvation number was small when the oxygen atom was close to the piperidinium ring. This difference suggests that the difference in the ring structure of the cation alters the coordination environment of the Li ions in RTILs.

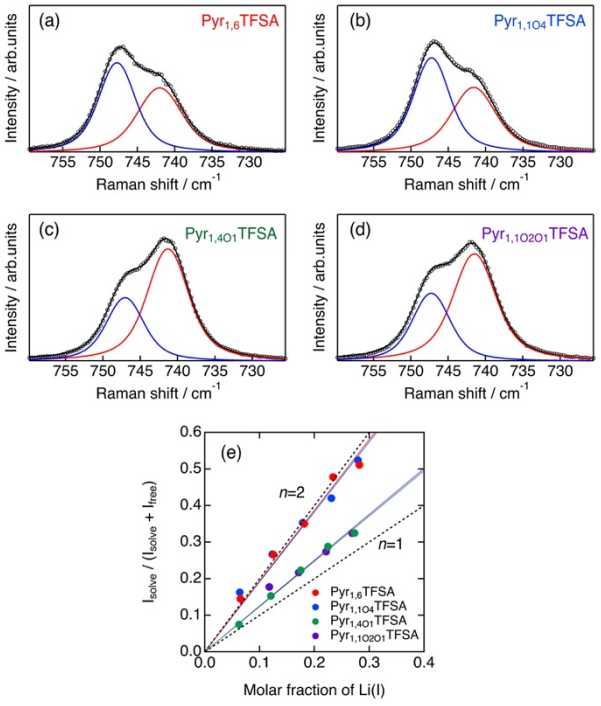

Figure 11. Raman spectra of (a) Pyr$_{1,6}$TFSA, (b) Pyr$_{1,1O4}$TFSA, (c) Pyr$_{1,4O1}$TFSA, and (d) Pyr$_{1,1O2O1}$TFSA in the presence of 1.0 M LiTFSA. The spectra were recorded between 725 and 760 cm^{-1}. The black circle and the black, red, and blue lines correspond to the observed spectrum, the fitted spectrum, and the deconvoluted components of the free and solvated $TFSA^-$, respectively. (e) Plot of $I_{solve}/(I_{solve}+I_{free})$ against the molar fraction of Li(I). The molar fraction of Li(I) was calculated from the density at 298 K.

To further understand the coordination environment of the Li ions in the RTILs containing ether oxygen atoms, MD calculations were conducted using 700 pyrrolidinium cations, 300 lithium ions, and 1,000 $TFSA^-$ ions. Figure 12 shows the RDF profiles of the cation (side chain)-Li ion interactions for the four RTILs based on MD trajectories of 1 μs, where a clear peak at ~0.8 nm can be observed in each case. This suggests that the majority of Li ions in the RTILs are considered to be in a similar coordination environment regardless of the type of cation. Interestingly, the RDF profiles at shorter distances were found to be dependent on the type of cation. More specifically, the profiles of $Pyr_{1,4O1}TFSA$ and $Pyr_{1,1O2O1}TFSA$ showed a peak at ~0.2 nm, while $Pyr_{1,6}TFSA$ and $Pyr_{1,1O4}TFSA$ did not. This is consistent with the result of the solvation number analysis obtained by Raman spectroscopy. An MD snapshot obtained from the calculation for $(Pyr_{1,1O2O1})_{0.7}Li_{0.3}TFSA$ is given in Fig. 12, which shows the interaction between the Li ion and the ether oxygen atom in the side chain (see also Fig. S6). From both the Raman measurements and the MD calculations, it was clarified that the coordination environment of Li ion was likely to be affected by the ether oxygen atom located away from the pyrrolidinium ring. In the case of $Pyr_{1,1O4}TFSA$, the ether oxygen atom did not affect the coordination environment of the Li ion due to the fact that the oxygen is located close to the pyrrolidinium ring, thereby rendering it sterically inaccessible to the Li ions. Compared with $Pyr_{1,4O1}TFSA$, $Pyr_{1,1O2O1}TFSA$ possesses a higher conformational flexibility and a larger negative charge on the oxygen atom, which may facilitate the interaction with Li ions (Fig. S7).

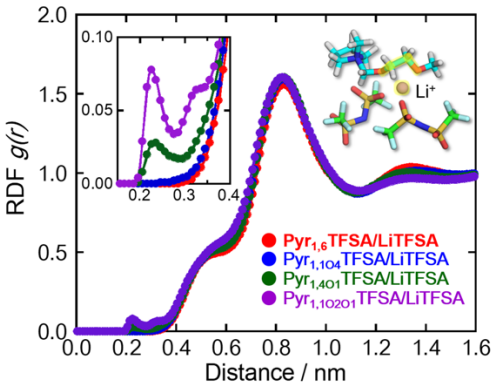

Figure 12. Radial distribution function *g(r)* involving the cation (side chain)-Li^+ interaction between the highlighted segments for the four RTILs, as determined from MD trajectories of 1 μs.

3. Conclusion

The physicochemical properties of ether-functionalized pyrrolidinium-based room temperature ionic liquids (RTILs) were investigated *via* both experimental and computational chemistry approaches. The introduction of ether oxygen atoms into the side chains of the RTILs resulted in a decreased viscosity and an enhanced ionic conductivity. For example, $Pyr_{1,1O2O1}TFSA$, which contains two oxygen atoms in its side chain, exhibited the lowest viscosity among the four RTILs examined herein. In the cases of $Pyr_{1,1O4}TFSA$ and $Pyr_{1,4O1}TFSA$, which possess the same molecular weight but where the oxygen atom is present at a different position in each, a lower viscosity and higher ionic conductivity were obtained for $Pyr_{1,1O4}TFSA$. *Ab initio* calculations revealed that the biggest difference in the potential energy barrier of the dihedral angle was observed at Φ_1, which corresponds to the root of the cation side chain. When the ether oxygen atom is located close to the pyrrolidinium ring, i.e., in $Pyr_{1,1O4}TFSA$ and $Pyr_{1,1O2O1}TFSA$, the potential barrier of Φ_1 is smaller, which may account for their good transport properties. Furthermore, radial distribution function (RDF) analysis obtained from molecular dynamics (MD) calculations at 300 K indicated that a regular arrangement of ions was found in $Pyr_{1,6}TFSA$ and $Pyr_{1,4O1}TFSA$, while this regularity was disturbed in $Pyr_{1,1O4}TFSA$ and $Pyr_{1,1O2O1}TFSA$ due to the flexibility of the side chain. This may also be a factor in determining the transport properties. These results therefore confirmed that the introduction of ether oxygen atoms into the position close to the pyrrolidinium ring is important in the design of RTILs with lower viscosities. Disrupting the ion arrangement is also essential to improving the transport properties, and systematic investigations into the effects of various substituents will be necessary in the future. The coordination environment of the Li ion in each RTIL was then investigated by Raman spectroscopy, and it was found that the coordination environment changed upon interaction with the ether oxygen atom when this ether oxygen was present far from the pyrrolidinium ring. MD calculations with 1000 ion pairs confirmed the interaction between the ether oxygen atom and the Li ion in $Pyr_{1,4O1}TFSA$ and $Pyr_{1,1O2O1}TFSA$. Due to the interaction between the cation with ether oxygen atoms in the side chain and the Li ion, the transport behavior of the Li ion under an electric field may be different from that of $[Li(TFSA)_2]^-$, as has been reported.[48] This point is very interesting from the viewpoint of physical chemistry, and we plan to work on the analysis. Also, since it is well known that the coordination environment of the metal ion in the electrolyte alters the electrochemical reaction, understanding this interaction is important in the context of electrolyte design. We therefore believe that the knowledge obtained during this study will be useful in the design of ionic liquids for a variety of applications. The application of these RTILs in the area of electrochemistry is currently under investigation in our group, and the results will be reported in due course.

Experimental Section

Preparation of the RTILs

1-Methylpyrroridine (>98%) 1-chlorohexane (>95%), and chlorotrimethylsilane (>98%) were purchased from Tokyo Chemical Industry Co., Ltd. . 1-butanol (>99%), calcium chloride (>99%), paraformaldehyde (>90%), 2-methoxyethoxymethyl chloride (>97%), and activated carbon (Darco® G-60) were purchased from FUJIFILM Wako Pure Chemicals Co., Ltd. 1-Bromo-4-methoxybutane (>99%) was purchased from Oakwood Products. Lithium bis(trifluoromethylsulfonyl)amide (LiTFSA) was obtained from Kanto Chemical Co., Ltd. Activated alumina (neutral, Brockmann I) was purchased from Sigma-Aldrich.
The RTILs were prepared following a previously described literature method with some modifications.[22, 49] Characterization of the obtained products was performed using NMR spectroscopy (JHM-ECS series, JEOL, $\nu(^1H)$ = 400 MHz) with tetramethylsilane as an internal reference. Obtained NMR spectra were shown in Figs. S8-11. The water contents of the RTILs were <20 ppm, as determined by Karl Fisher titrations (Kyoto Electronics Manufacturing, MKC-610). After preparation, all RTILs were stored and handled in an argon-filled glove box equipped with a continuous

gas purification system (MDB-1NKPS, Miwa MFG Co. Ltd., H_2O and O_2 <1 ppm). The details of the synthesis procedure are described below, and the schemes are shown in Scheme S1 to S4.

1-Hexyl-1-methylpyrrolidinium bis(trifluoromethylsulfonyl)amide ($Pyr_{1,6}TFSA$)

1-Chlorohexane and 1-methylpyrroridine were added to acetonitrile and the resulting mixture was stirred for 12 h at 80 °C. After cooling to room temperature, ethyl acetate was added to form a precipitate, which was recrystallized 3 times with acetonitrile and ethyl acetate. The obtained 1-hexyl-1-methylpyrrolidinium chloride ($Pyr_{1,6}Cl$) was dried under vacuum at 100 °C, then mixed with LiTFSA in distilled water at room temperature to yield $Pyr_{1,6}TFSA$. $Pyr_{1,6}TFSA$ was then extracted into dichloromethane and washed with distilled water several times. After drying of the organic phase under vacuum at 100 °C for 24 h, $Pyr_{1,6}TFSA$ was obtained as a colorless liquid. ^1H NMR (400 MHz, $CDCl_3$) δ 0.90 (t, 3H), 1.33 (m, 6H), 1.75 (m, 2H), 2.26 (m, 4H), 3.04 (m, 3H), 3.30 (m, 2H), 3.51 (m, 4H); ^{13}C NMR (100 MHz, $CDCl_3$) δ 13.8, 21.5, 22.3, 23.7, 25.8, 31.0, 48.3, 64.6, 77.1, 119.8 (q). Elemental analysis calculated (%) for $C_{13}H_{24}F_6N_2O_4S_2$: C 34.66, H5.37, N 6.22; found: C 34.49, H 5.35, N 6.26.

1-(Butoxymethyl)-1-methylpyrrolidinium bis(trifluoromethylsulfonyl)amide ($Pyr_{1,1O4}TFSA$)

1-Butanol, calcium chloride, and paraformaldehyde were added to anhydrous dichloromethane under a nitrogen atmosphere at 0 °C and stirred for 15 min. After this time, chlorotrimethylsilane was added slowly to the mixture using a dropping funnel at 0 °C. After stirring for 30 min, the reaction mixture was filtered, and the solvent was removed under a vacuum. The resulting crude solution was distilled to obtain 1-(chloromethoxy)butane. Subsequently, 1-methylpyrrolidine was added slowly to a dichloromethane solution of 1-(chloromethoxy)butane at 0 °C under a nitrogen atmosphere with constant stirring. After stirring for 1.5 h, the solvent was removed under vacuum. The crude product was then washed with diethyl ether and mixed with methanol and activated carbon. After stirring for 1.5 h at room temperature, the activated carbon was removed by filtration, and methanol was distilled off. The obtained 1-(butoxymethyl)-1-methylpyrrolidinium chloride ($Pyr_{1,1O4}Cl$) was dried under vacuum, then mixed with LiTFSA in distilled water at room temperature to yield $Pyr_{1,1O4}TFSA$. Thus $Pyr_{1,1O4}TFSA$ was then extracted into dichloromethane and washed with distilled water several times. The resulting $Pyr_{1,1O4}TFSA$ was dissolved in ethyl acetate, treated with activated carbon, and filtered. $Pyr_{1,1O4}TFSA$ was finally obtained as a colorless liquid after drying under vacuum at 80 °C for 24 h. ^1H NMR (400 MHz, $CDCl_3$) δ 0.93 (t, 3H), 1.38 (m, 2H), 1.62 (m, 2H), 2.23 (m, 4H), 3.07 (s, 3H), 3.40 (m, 2H), 3.60 (m, 2H), 3.77 (t, 2H), 4.56 (s, 2H); ^{13}C NMR (100 MHz, $CDCl_3$) δ 13.5, 18.8, 22.1, 31.3, 47.5, 61.1, 72.8, 77.3, 89.5, 119.8 (q). Elemental analysis calculated (%) for $C_{12}H_{22}F_6N_2O_5S_2$: C 31.86, H4.90, N 6.19; found: C 31.71, H 4.88, N 6.22.

1-(4-Methoxybutyl)-1-methyl pyrrolidinium bis(trifluoromethylsulfonyl)amide ($Pyr_{1,4O1}TFSA$) and 1-((2-methoxyethoxy)methyl)-1-methylpyrrolidinium bis(trifluoromethylsulfonyl)amide ($Pyr_{1,1O2O1}TFSA$)

1-Bromo-4-methoxybutane or 2-methoxyethoxymethyl chloride was added slowly to an acetonitrile solution of 1-methylpyrrolidine at 0 °C under a nitrogen atmosphere with constant stirring. After stirring for 12 h at ambient temperature, the solvent in the reaction mixture was removed under vacuum. The crude product was then washed with ethyl acetate several times, and the obtained 1-(4-methoxybutyl)-1-methyl pyrrolidinium bromide ($Pyr_{1,4O1}Br$) or 1-((2-methoxyethoxy)methyl)-1-methylpyrrolidinium chloride ($Pyr_{1,1O2O1}Cl$) was dried under vacuum at 100 °C for 24 h. After this time, reaction with LiTFSA in distilled water at 25 °C yielded $Pyr_{1,4O1}TFSA$ or $Pyr_{1,1O2O1}TFSA$. $Pyr_{1,4O1}TFSA$ or $Pyr_{1,1O2O1}TFSA$ was then extracted into dichloromethane and washed with distilled water several times. The resulting liquid was dissolved in ethyl acetate, treated with the activated carbon, and filtered. Following treatment with activated alumina and filtration, the excess ethyl acetate was removed using a rotary evaporator. $Pyr_{1,4O1}TFSA$ or $Pyr_{1,1O2O1}TFSA$ was finally obtained as a colorless liquid after drying the residue under vacuum at 80 °C for 24 h. ^1H NMR (400 MHz, $CDCl_3$) of $Pyr_{1,4O1}TFSA$: δ 1.64 (m, 2H), 1.86 (m, 2H), 2.26 (m, 4H), 3.04 (s, 3H), 3.32-3.37 (m, 5H), 3.42 (t, 2H), 3.51 (m, 4H); ^{13}C NMR (100 MHz, $CDCl_3$) of $Pyr_{1,4O1}TFSA$: δ 21.0, 21.4, 26.0, 48.4, 58.5, 64.5, 71.3, 77.1, 119.8 (q). Elemental analysis calculated (%) for $C_{12}H_{22}F_6N_2O_5S_2$: C 31.86, H4.90, N 6.19; found: C 31.66, H 4.96, N 6.06. ^1H NMR (400 MHz, $CDCl_3$) of $Pyr_{1,1O2O1}TFSA$: δ 2.23 (m, 4H), 3.09 (s, 3H), 3.36-3.46 (m, 5H), 3.54-3.70 (m, 4H), 3.94 (m, 2H), 4.65 (m, 2H); ^{13}C NMR (100 MHz, $CDCl_3$) of $Pyr_{1,1O2O1}TFSA$: δ 22.0, 47.5, 58.9, 61.2, 71.5, 72.4, 77.1, 89.8, 119.8 (q). Elemental analysis calculated (%) for $C_{11}H_{20}F_6N_2O_6S_2$: C 29.08, H4.44, N 6.17; found: C 28.92, H 4.48, N 6.07.

Measurement of the physicochemical properties

The melting and glass transition temperatures were measured by differential scanning calorimetry (SII nanotechnology, DSC6220) in a sealed-aluminum ampoule at a rate of 5 K min^{-1}. A series of viscosity measurements were carried out using a viscometer (Kyoto Electronics, EMS-1000S), and the densities were measured using a vibrating-type densitometer (Anton Paar, DMA™ 4500). The ionic conductivity was measured using an airtight four-probe conductivity cell consisting of two inner platinum wire electrodes (1.0 mm diameter) to monitor the potential difference, and two outer platinum disk-electrodes (13.0 mm diameter) for feeding an alternating current amplitude of 10 mV using a potentiostat/galvanostat (Hokuto, HZ-7000) after cell calibration using a standard KCl aqueous solution (Kishida Chemical, 7 mS cm^{-1} at 25 °C). A Raman spectroscopy system (InVia Raman Spectrometer, Renishaw Plc.) equipped with a 532 nm Nd:YAG laser was used to analyze the coordination environments of the Li ions in the RTILs. The samples for measurement were prepared in an argon-filled glove box, and the measurements were carried out without exposing the samples to air.

Computational methods

The pyrrolidinium cations were investigated by *ab initio* quantum mechanics (QM) calculations to evaluate the three-dimensional structures of the side chains. Conformational analysis was performed on the dihedral angles (Φ_1, Φ_2, Φ_3, and Φ_4) as shown in Fig. S2. The cation structures were optimized using the MP2/6-31G(d,p) level of theory while increasing the dihedral angle Φ from −180 to 180° in 15° steps and with three conformations (60, −60, and 180°) for the remaining dihedral angles. Taking into account the two conformations for C-N-C-X (60 and −60°), 5,400 structures were finally generated. Structure optimization was then performed with a fixed dihedral angle Φ to estimate the torsional potential energy. The profiles of the potential energy surfaces were obtained by single-point calculations at the MP2/aug-cc-pVTZ level of theory for the optimized structures.

The molecular dynamics (MD) calculations were performed on the four pyrrolidinium-based RTILs (Fig. 1) at a constant temperature (300 K) and pressure (1 bar). The MD systems of the pyrrolidinium-based RTILs consist of 1,000 or 5,000 ion pairs in a rectangular periodic box. MD simulation of the 1,000 ion pairs was performed for 1 μs, and the MD trajectory was used to analyze the structural geometry and ion distribution. In contrast, the MD simulation of the 5,000 ion pairs was carried out to evaluate the mean-square-displacements (MSDs), which required sufficient sampling. In our previous study, the parameter set of pyrrolidinium-based RTILs was developed by modifying the general AMBER force field (GAFF).[22, 50] The AMBER potential is described in terms of the following equation: [51]

$$V_{\mathrm{AMBER}} = \sum_{bonds} K_r\left(r - r_{eq}\right)^2 + \sum_{angles} K_\theta\left(\theta - \theta_{eq}\right)^2 + \sum_{dihedrals} \frac{V_n}{2}\left[1 + \cos(n\phi - \gamma)\right] + \sum_{impropers} K_x\left(x - x_{eq}\right)^2 + \sum_{i<j} \frac{q_i q_j}{4\pi\varepsilon_0 R_{ij}} + \sum_{i<j} 4\varepsilon_{ij}\left[\left(\frac{\sigma_{ij}}{R_{ij}}\right)^{12} - \left(\frac{\sigma_{ij}}{R_{ij}}\right)^{6}\right]$$

The atomic charge parameters (q) for the pyrrolidinium-based RTILs were assigned based on the restrained electrostatic potential (RESP)[52, 53], and they were adjusted to 80% scale to reproduce the physical properties.[54–56] Tables X1–X4 list the non-bonded interaction parameters of the pyrrolidinium-based cations. The parameters of the dihedral angle for the pyrrolidinium-based cations were set to those previously developed (Table X5). The remainder of the parameters were taken from the original GAFF force field. The detailed conditions for the MD simulation followed those reported in a previous study.[22]

The MD simulation for the mixed system of pyrrolidinium-based RTILs and LiTFSA was also performed for 1 μs under a constant temperature (300 K) and pressure (1 bar). The mixed system consists of 700 pyrrolidinium cations, 300 lithium ions, and 1,000 $TFSA^-$. As in the case of the non-bonded interaction parameter of the Li ion, the atomic charge was set to 0.8, and the 12-6 ion-oxygen distance (IOD) set was assigned to the van der Waals parameters.[57,58] The QM calculations were performed using Gaussian 09 Rev. C01 software.[59] The MD calculations were carried out using the PMEMD.CUDA module of the Amber 18 package with the NVIDIA® Pascal GPU system.[60–62] The MD system of the pyrrolidinium-based RTILs was generated using the Packmol 16.103 package.[63] The MD trajectory analysis was performed using the CPPTRAJ module[64] of AmberTools 19. The molecular graphics software, PyMOL 1.7.1 (Schrödinger LLC)[65] was employed to display the QM and MD structures.

Acknowledgements

Part of this research was supported by the Japan Society for the Promotion of Science (JSPS KAKENHI Grant Numbers 19K15686). The QM and MD calculations were partly carried out using the computer resource offered under the category of Intensively Promoted Projects by Research Institute for Information Technology, Kyushu University.

Keywords: ionic liquid, molecular dynamics, ether functionalization, physicochemical properties, Li coordination

[1] M. Armand, F. Endres, D. R. MacFarlane, H. Ohno, B. Scrosati, *Nat. Mater.* **2009**, *8*, 621-629.
[2] T. Torimoto, T. Tsuda, K.-i. Okazaki, S. Kuwabata, *Adv. Mater.* **2010**, *22*, 1196-1221.
[3] H. Ohno, Electrochemical Aspects of Ionic Liquids, Wiley, Inc, Hoboken, NJ, **2011**.
[4] D. R. MacFarlane, N. Tachikawa, M. Forsyth, J. M. Pringle, P. C. Howlett, G. D. Eliott, J. Davis, James H., M. Watanabe, P. Simon, C. A. Angell, *Energy Environ. Sci.* **2014**, *7*, 232-250.
[5] C. F. J. Francis, I. L. Kyratzis, A. S. Best, *Adv. Mater.* **2020**, *32*, e1904205.
[6] F. Ren, J. Wang, F. Xie, K. Zan, S. Wang, S. Wang, *Green Chem.* **2020**, *22*, 2162-2183.
[7] S. K. Singh, A. W. Savoy, *J. Mol. Liq.* **2020**, *297*.
[8] D. R. MacFarlane, P. Meakin, J. Sun, M. Forsyth, *J. Phys. Chem. B*. **1999**, *103*, 4164-4170.
[9] H. Tokuda, K. Ishii, M. A. Susan, S. Tsuzuki, K. Hayamizu, M. Watanabe, *J. Phys. Chem. B*. **2006**, *110*, 2833-2839.
[10] S. Yamaguchi, H. Yamada, Y. Takeoka, M. Rikukawa, M. Yoshizawa-Fujita, *New J. Chem.* **2019**, *43*, 4008-4012.
[11] M. Ishikawa, T. Sugimoto, M. Kikuta, E. Ishiko, M. Kono, *J. Power Sources.* **2006**, *162*, 658-662.
[12] K. Yoshii, T. Masese, M. Kato, K. Kubota, H. Senoh, M. Shikano, *ChemElectroChem*. **2019**, *6*, 3901-3910.
[13] Z.-B. Zhou, H. Matsumoto, K. Tatsumi, *Chem. Eur. J.* **2006**, *12*, 2196-2212.
[14] Z. Fei, W. H. Ang, D. Zhao, R. Scopelliti, E. E. Zvereva, S. A. Katsyuba, P. J. Dyson, *J. Phys. Chem. B*. **2007**, *111*, 10095-10108.
[15] G. D. Smith, O. Borodin, L. Li, H. Kim, Q. Liu, J. E. Bara, D. L. Gin, R. D. Noble, *Phys. Chem. Chem. Phys*. **2008**, *10*, 6301-6312.
[16] Z. J. Chen, T. Xue, J.-M. Lee, *RSC Advances*. **2012**, *2*, 10564-10574.
[17] T. Makino, M. Kanakubo, T. Umecky, A. Suzuki, *J. Chem. Eng. Data.* 2013, 58, 370-376.
[18] M. Kunze, E. Paillard, S. Jeong, G. B. Appetecchi, M. Schönhoff, M. Winter, S. Passerini, *J. Phys. Chem. C*. **2011**, *115*, 19431-19436.
[19] J. von Zamory, G. A. Giffin, S. Jeremias, F. Castiglione, A. Mele, E. Paillard, S. Passerini, *Phys. Chem. Chem. Phys*. **2016**, *18*, 21539-21547.
[20] S. I. Lall-Ramnarine, M. Zhao, C. Rodriguez, R. Fernandez, N. Zmich, E. D. Fernandez, S. B. Dhiman, E. W. Castner, J. F. Wishart, *J. Electrochem. Soc.* **2017**, *164*, H5247-H5262.
[21] A. Tsurumaki, F. Trequattrini, O. Palumbo, S. Panero, A. Paolone, M. A. Navarra, *Phys. Chem. Chem. Phys*. **2018**, *20*, 7989-7997.
[22] K. Yoshii, T. Uto, N. Tachikawa, Y. Katayama, *Phys. Chem. Chem. Phys.* **2020**, *22*, 19480-19491.
[23] F. Philippi, D. Rauber, B. Kuttich, T. Kraus, C. W. M. Kay, R. Hempelmann, P. A. Hunt, T. Welton, *Phys. Chem. Chem. Phys*. **2020**, *22*, 23038-23056.
[24] G. A. Giffin, A. Moretti, S. Jeong, K. Pilar, M. Brinkkotter, S. G. Greenbaum, M. Schonhoff, S. Passerini, *ChemSusChem*. **2018**, *11*, 1981-1989.
[25] M. Shimizu, K. Yamaguchi, H. Usui, N. Ieuji, T. Yamashita, T. Komura, Y. Domi, T. Nokami, T. Itoh, H. Sakaguchi, *J. Electrochem. Soc.* **2020**, *167*.
[26] J. Atik, D. Diddens, J. H. Thienenkamp, G. Brunklaus, M. Winter, E. Paillard, *Angew. Chem. Int. Ed.* **2021**, *60*, 11919-11927.
[27] J. C. Lassegues, J. Grondin, D. Talaga, *Phys. Chem. Chem. Phys*. **2006**, *8*, 5629-5632.
[28] Y. Umebayashi, T. Yamaguchi, S. Fukuda, T. Mitsugi, M. Takeuchi, K. Fujii, S. Ishiguro, *Anal. Sci.* **2008**, *24*, 1297-1304.
[29] S. Duluard, J. Grondin, J.-L. Bruneel, I. Pianet, A. Grélard, G. Campet, M.-H. Delville, J.-C. Lassègues, *J. Raman Spectrosc*. **2008**, *39*, 627-632.
[30] M. Kar, B. Winther-Jensen, M. Forsyth, D. R. MacFarlane, *Phys. Chem. Chem. Phys.* **2013**, *15*, 7191-7197.
[31] G. A. Giffin, J. Tannert, S. Jeong, W. Uhl, S. Passerini, *J. Phys. Chem. C*. **2015**, *119*, 5878-5887.
[32] T. Watkins, A. Kumar, D. A. Buttry, *J. Am. Chem. Soc*. **2016**, *138*, 641-650.
[33] X. Gao, X. Liu, A. Mariani, G. A. Elia, M. Lechner, C. Streb, S. Passerini, *Energy Environ. Sci.* **2020**.
[34] C. Comminges, R. Barhdadi, M. Laurent, M. Troupel, *J. Chem. Eng. Data*. **2006**, *51*, 680-685.
[35] T. Nokami, K. Matsumoto, T.-a. Itoh, Y. Fukaya, T. Itoh, *Org. Process Res. Dev*. **2014**, *18*, 1367-1371.
[36] K. Shimizu, C. E. Bernardes, A. Triolo, J. N. Canongia Lopes, *Phys. Chem. Chem. Phys.* **2013**, *15*, 16256-16262.
[37] A. J. Easteal, C. A. Angell, *J. Chem. Phys.* 1972, 56, 4231-4233.
[38] W. Xu, E. I. Cooper, C. A. Angell *J. Phys. Chem. B*. **2003**, *107*, 6170-6178.
[39] Y. Umebayashi, T. Mitsugi, K. Fujii, S. Seki, K. Chiba, H. Yamamoto, J. N. C. Lopes, A. A. H. Padua, M. Takeuchi, R. Kanzaki, S. Ishiguro, *J. Phys. Chem. B*. **2009**, *113*, 4338-4346.
[40] B. Ganguly, B. Fuchs, *J. Org. Chem.* **2000**, *65*, 558-561.
[41] A. S. L. Gouveia, C. E. S. Bernardes, E. I. Lozinskaya, A. S. Shaplov, J. N. Canongia Lopes, I. M. Marrucho, *Phys. Chem. Chem. Phys.* **2019**, *21*, 23305-23309.
[42] K. Fujii, T. Nonaka, Y. Akimoto, Y. Umebayashi, S. Ishiguro, *Anal. Sci.* **2008**, *24*, 1377-1380.
[43] M. Kunze, S. Jeong, E. Paillard, M. Schönhoff, M. Winter, S. Passerini, *Adv. Energy Mater.* **2011**, *1*, 274-281.

[44] F. Castiglione, A. Famulari, G. Raos, S. V. Meille, A. Mele, G. B. Appetecchi, S. Passerini, *J. Phys. Chem. B*. **2014**, *118*, 13679-13688.
[45] K. Pilar, V. Baledent, M. Zeghal, P. Judeinstein, S. Jeong, S. Passerini, S. Greenbaum, *J. Chem. Phys.* **2018**, *148*, 031102.
[46] M. Shimizu, H. Usui, H. Sakaguchi, *Phys. Chem. Chem. Phys*. **2016**, *18*, 5139-5147.
[47] S. Menne, T. Vogl, A. Balducci, *Phys. Chem. Chem. Phys.* **2014**, *16*, 5485-5489.
[48] M. Gouverneur, F. Schmidt, M. Schönhoff, *Phys. Chem. Chem. Phys.* **2018**, *20*, 7470-7478.
[49] T. Nokami, T. Yamashita, T. Komura, N. Handa, M. Shimizu, K. Yamaguchi, Y. Domi, H. Usui, H. Sakaguchi, T. Itoh, *Faraday Discuss.* **2018**, *206*, 523-534.
[50] J. Wang, R. M. Wolf, J. W. Caldwell, P. A. Kollman, D. A. Case, *J. Comput. Chem.* **2004**, *25*, 1157–1174.
[51] W. D. Cornell, P. Cieplak, C. I. Bayly, I. R. Gould, K. M. Merz, D. M. Ferguson, D. C. Spellmeyer, T. Fox, J. W. Caldwell, P. A. Kollman, *J. Am. Chem. Soc.* **1995**, *117*, 5179-5197.
[52] C. I. Bayly, P. Cieplak, W. Cornell, P. A. Kollman, *J. Phys. Chem.* **1993**, *97*, 10269-10280.
[53] W. D. Cornell, P. Cieplak, C. I. Bayly, P. A. Kollman, *J. Am. Chem. Soc.* **1993**, *115*, 9620-9631.
[54] C. M. Tenney, M. Massel, J. M. Mayes, M. Sen, J. F. Brennecke, E. J. Maginn, *J. Chem. Eng. Data*. **2014**, *59*, 391-399.
[55] K. G. Sprenger, V. W. Jaeger, J. Pfaendtner, *J. Phys. Chem. B*. **2015**, *119*, 5882-5895.
[56] T. Uto, K. Yamamoto, J. Kadokawa, *J. Phys. Chem. B*. **2018**, *122*, 258–266.
[57] P. Li, L. F. Song, K. M. Merz, Jr., *J. Chem. Theory Comput.* **2015**, *11*, 1645-1657.
[58] P. Ray, A. Balducci, B. Kirchner, *J Phys Chem B*. **2018**, *122*, 10535-10547.
[59] M. J. Frisch, G. W. Trucks, H. B. Schlegel, G. E. Scuseria, M. A. Robb, J. R. Cheeseman, G. Scalmani, V. Barone, B. Mennucci, G. A. Petersson, H. Nakatsuji, M. Caricato, X. Li, H. P. Hratchian, A. F. Izmaylov, J. Bloino, G. Zheng, J. L. Sonnenberg, M. Hada, M. Ehara, K. Toyota, R. Fukuda, J. Hasegawa, M. Ishida, T. Nakajima, Y. Honda, O. Kitao, H. Nakai, T. Vreven, J. A. Montgomery, J. E. Peralta, F. Ogliaro, M. Bearpark, J. J. Heyd, E. Brothers, K. N. Kudin, V. N. Staroverov, R. Kobayashi, J. Normand, K. Raghavachari, A. Rendell, J. C. Burant, S. S. Iyengar, J. Tomasi, M. Cossi, N. Rega, J. M. Millam, M. Klene, J. E. Knox, J. B. Cross, V. Bakken, C. Adamo, J. Jaramillo, R. Gomperts, R. E. Stratmann, O. Yazyev, A. J. Austin, R. Cammi, C. Pomelli, J. W. Ochterski, R. L. Martin, K. Morokuma, V. G. Zakrzewski, G. A. Voth, P. Salvador, J. J. Dannenberg, S. Dapprich, A. D. Daniels, Farkas, J. B. Foresman, J. V. Ortiz, J. Cioslowski, D. J. Fox in Gaussian 09, Revision C. 01, **2009**.
[60] R. Salomon-Ferrer, A. W. Gotz, D. Poole, S. Le Grand, R. C. Walker, *J. Chem. Theory Comput.* **2013**, *9*, 3878–3888.
[61] S. Le Grand, A. W. Götz, R. C. Walker, *Comput. Phys. Commun.* **2013**, *184*, 374–380.
[62] D. A. Case, I. Y. Ben-Shalom, S. R. Brozell, D. S. Cerutti, T. E. Cheatham III, V. W. D. Cruzeiro, T. A. Darden, R. E. Duke, D. Ghoreishi, M. K. Gilson, H. Gohlke, A. W. Goetz, D. Greene, R. Harris, N. Homeyer, Y. Huang, S. Izadi, A. Kovalenko, T. Kurtzman, T. S. Lee, S. LeGrand, P. Li, C. Lin, J. Liu, T. Luchko, R. Luo, D. J. Mermelstein, K. M. Merz, Y. Miao, G. Monard, C. Nguyen, H. Nguyen, I. Omelyan, A. Onufriev, F. Pan, R. Qi, D. R. Roe, A. Roitberg, C. Sagui, S. Schott-Verdugo, J. Shen, C. L. Simmerling, J. Smith, R. Salomon-Ferrer, J. Swails, R. C. Walker, J. Wang, H. Wei, R. M. Wolf, X. Wu, L. Xiao, D. M. York, P. A. Kollman in Amber 18, **2018**.
[63] L. Martinez, R. Andrade, E. G. Birgin, J. M. Martinez, *J. Comput. Chem.* **2009**, *30*, 2157–2164.
[64] D. R. Roe, T. E. Cheatham, III, *J. Chem. Theory Comput.* **2013**, *9*, 3084–3095.
[65] Schödinger LLC. in The PyMOL molecular graphics system, ver. 1.7.1.0, Schödinger LLC., **2014**.

Entry for the Table of Contents

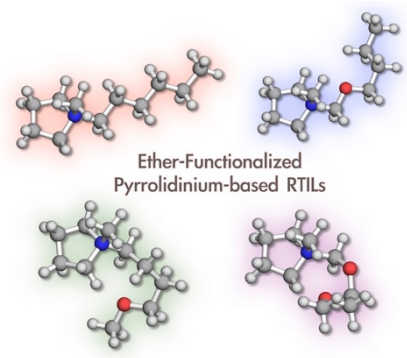

The physicochemical properties of ether-functionalized pyrrolidinium-based room temperature ionic liquids were investigated using both experimental and computational approaches. The position and number of the ether oxygen atom had an impact on the physicochemical properties, as discussed in detail using molecular dynamics calculations and careful comparison with experimental results. The coordination environments of the Li ions in the ionic liquids were also investigated.